ACS APPLIED MATERIALS & INTERFACES

Research Article

www.acsami.org

Controlled Synthesis of Mesoporous MnO/C Networks by Microwave Irradiation and Their Enhanced Lithium-Storage Properties

Wei Luo, Xianluo Hu,* Yongming Sun, and Yunhui Huang*

State Key Laboratory of Material Processing and Die & Mould Technology, School of Materials Science and Engineering, Huazhong University of Science and Technology, Wuhan 430074, People's Republic of China

Supporting Information

ABSTRACT: A rapid and controllable route is developed for the synthesis of MnO nanoparticles that are encapsulated uniformly in three-dimensional (3D) mesoporous interconnected carbon networks (MnO-MICN) through an efficient microwave-polyol process, combined with a subsequent thermal treatment. The dependence of sodium citrate on the morphology of the Mn-based precursors was investigated systematically. Results show that the unique mesoporous interconnected carbon network (MICN) can not only buffer the large volume expansion of MnO during the electrochemical cycling, but also improve the electrode/electrolyte contact area, favoring the fast Li-ion transport and high specific capacity, superior cyclability, and excellent rate capability. When evaluated as an anode material for lithium-ion batteries, the as-formed 3D MnO-MICN nanocomposite exhibits a highly reversible capacity of 1224 mA h g^{-1}, with a Coulombic efficiency of ~99% at a current density of 200 mA g^{-1} over 200 cycles.

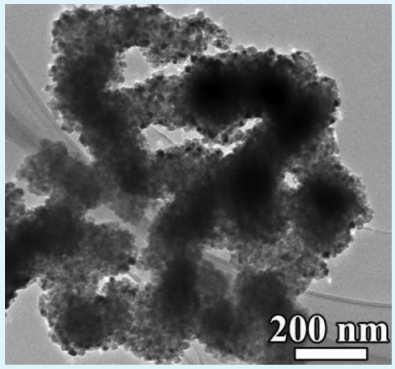

KEYWORDS: *nanocomposite, mesoporous, microwave irradiation, anode, lithium-ion batteries*

INTRODUCTION

Over the past decades, lithium-ion batteries (LIBs) have been explored as the optimal power source for portable electronics and implantable medical devices, and they are now being extended to forthcoming electric vehicles.[1−3] Unfortunately, graphite, which is the current conventional anode material for LIBs, cannot meet the increasing demands for large energy and power density, because of its limited theoretical capacity of 372 mAh g^{-1}. Recent tendencies have been toward high-capacity substitutes for graphite, such as silicon,[4] tin,[5,6] and transition-metal oxides (TMOs).[7−12] Among the TMOs, MnO has been recognized as one of the most promising anode materials for LIBs, because of its high theoretical capacity (755 mA h g^{-1}), relatively low voltage hysteresis, low cost, and nontoxicity, which is expected to meet the requirements of future LIBs.[13,14] During the discharge/charge cycling, however, MnO is usually reduced to tiny Mn clusters based on a conversion reaction, and meanwhile Li_2O is formed by reacting oxygen with Li ions. Large volume expansion and severe collapse of the electrode may occur upon cycling, thus inevitably resulting in rapid capacity fading. In addition, the poor electronic conductivity of MnO limits its wide applications.[15] Recently, considerable efforts have been made to address this issue, including the use of nanosized active materials,[16,17] porous structures,[18,19] and hybridization with conductive materials (e.g., Co,[20] C,[21−23] and graphene[24−26]).

Very recently, the incorporation of conductive networks (e.g., nanonetworks of metal-rich phosphides,[27] carbon nanotubes,[28−30] or graphene[31−33]) into electrode materials has been deemed a promising strategy to improve both the structural stability and the electronic/ionic conductivity while enabling a high rate of performance and excellent cyclability. For instance, Maier and co-workers introduced hierarchical mixed-conducting networks into electrode materials for LIBs that exhibit significantly enhanced electrochemical performances.[34−36] Nevertheless, these composite conducting networks involve either expensive noble-metal oxides (RuO_2) or complex synthesis processes (carbon tube-in-tube). Therefore, controlled and fast production of high-performance conductive networks of high quality, serving as electrode materials for LIB applications, still remains a significant challenge.

Microwave irradiation offers an efficient strategy of heating that usually leads to higher yields and shorter reaction time. It has been demonstrated that microwave irradiation is becoming an increasingly popular heating method for functional materials synthesis. In particular, it is unique in providing scale-up processes with a uniform reaction environment, thus paving the way to the large-scale industrial production of high-quality nanostructured materials.[37−45] We have recently developed the microwave-enhanced routes for the preparation of colloidal α-Fe_2O_3 and ZnO nanocrystals with continuous size tuning and fine shape control in close aqueous systems, by taking advantage of microwave irradiation and hydrothermal effects.[43−45] In this work, we describe the rapid and controllable synthesis of MnO nanoparticles that are encapsulated uniformly in a three-dimensional (3D) mesoporous interconnected

Received: November 23, 2012
Accepted: February 22, 2013
Published: February 22, 2013

carbon network (MnO-MICN) through an efficient microwave-polyol process combined with a subsequent thermal treatment. The exposure time of microwave irradiation and the reaction temperature are programmed. The power of microwave heating is automatically adjusted. The reaction temperature is continuously monitored and controlled by the automatic temperature-control system. Importantly, the unique 3D mesoporous interconnected carbon network can not only buffer the large volume expansion of MnO during the electrochemical cycling, but also improve the electrode/electrolyte contact area, favoring the fast Li-ion transport and high specific capacity, superior cyclability, and excellent rate capability.

EXPERIMENTAL SECTION

Materials Synthesis. The 3D MnO-MICN sample was prepared in a microwave synthesis system (2.45 GHz, 300 W, Discover S-Class, CEM). The unique, circular single-mode cavity ensured that the reaction system was in a homogeneous, highly dense microwave field. The system was equipped with in situ magnetic stirring, and the glass reaction flask was fit with a 15-cm air-cooled condenser. The exposure time and temperature were programmed. The automatic temperature-control system allowed continuous monitoring and control of the internal temperature of the reaction systems. The preset profile (desired time and temperature) was followed automatically by continuously adjusting the applied microwave power. In a typical procedure, manganese acetate (MA, 2 mmol), and sodium citrate (SC, 0.6 mmol) were dissolved in 20 mL of ethylene glycol (EG). Then, the mixture solution was microwave-treated under magnetic stirring at 200 °C for 20 min to form a slightly pink turbid solution. The products were collected by centrifugation, washed with absolute ethanol, and dried in an oven at 80 °C overnight. The MnO-MICN product was finally obtained by annealing the as-synthesized slightly pink intermediate at 500 °C for 5 h in H_2 (5%)/Ar (2 °C min^{-1}). For comparison, free MnO nanoparticles were synthesized by directly thermally treating manganese acetate at 500 °C for 5 h in H_2 (5%)/Ar (2 °C min^{-1}).

Materials Characterization. Powder X-ray diffraction (XRD) patterns were collected with a PANalytical MultiPurpose Diffractometer, using high-intensity Cu Kα_1 radiation (λ = 1.5406 Å). The morphology and composition of the products were characterized using field-emission scanning electron microscopy (FESEM) (FEI, Model Sirion 200) with an energy-dispersive X-ray (EDX) attachment. Microstructural properties were obtained using transmission electron microscopy (TEM) (FEI, Model Tecnai-20) and high-resolution transmission electron microscopy (HRTEM) (JEOL, Model JEM2010F). X-ray photoelectron spectroscopy (XPS) measurements were carried out on a VG MultiLab 2000 system with a monochromatic Al Kα X-ray source (ThermoVG Scientific). The Raman spectra were recorded with a Renishaw Invia spectrometer, using an Ar^+ laser at 514.5 nm. The nitrogen adsorption/desorption isotherms were measured at 77 K on a Micrometritics ASAP 2020 analyzer. Thermogravimetric analysis (TGA) was performed on a Perkin–Elmer Model Pyris1 TGA apparatus at a heating rate of 10 °C min^{-1} in flowing air. Fourier-transform infrared (FT-IR) spectra were recorded on a Bruker VERTEX 70 FT-IR spectrometer.

Electrochemical Measurement. Electrochemical experiments were performed using 2032 coin-type half cells. The working electrode consists of the 3D MnO-MICN, Super P, and poly(vinyl difluoride) (PVDF) in a 70:20:10 weight ratio. A lithium pellet was used as the counter electrode, and 1 M solution of $LiPF_6$ in ethylene carbonate (EC)/dimethyl carbonate (DMC) was used as the electrolyte. An electrochemical workstation (Shaghai Chen Hua Instruments, Model CHI660D) was employed for cyclic voltammetry (CV) measurement at a scanning rate of 0.2 mV s^{-1} and electrochemical impedance spectrometry (EIS) tests in a frequency range from 100 kHz to 1 mHz at room temperature. Galvanostatic cycling was performed on a multichannel battery testing system (LANDdt BST5 V/5 mA) at room temperature.

RESULTS AND DISCUSSION

XRD patterns provide crystallinity and phase information for the products. As shown in Figure 1a, the XRD pattern of the

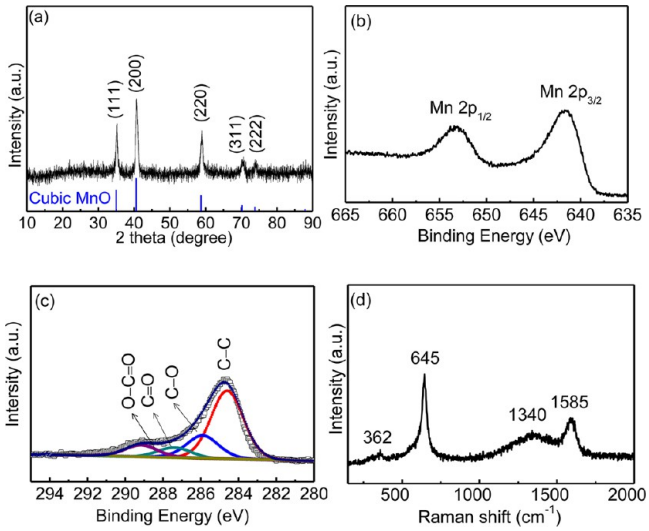

Figure 1. (a) XRD pattern, (b, c) XPS spectra, and (d) Raman spectrum of MnO-MICN.

MnO-MICN product can be readily indexed to a pure phase of cubic MnO (JCPDS File Card No. 78-0424). The crystalline size of these MnO nanoparticles is estimated to be ~14.2 nm, using the Scherrer formula, based on the (200) peak at 2θ = 40.7°. The composition and oxidation state of the MnO-MICN product were explored by XPS analysis. As shown in Figures 1b and 1c, the elemental manganese and carbon are generated from MnO and the carbon network. The XPS spectrum of Mn 2p displays peaks at 641.7 eV for Mn $2p_{3/2}$ and 653.4 eV for Mn $2p_{1/2}$, which is characteristic of MnO.[26] The high-resolution C 1s spectrum can be deconvolved into four peaks. The strong peak centered at 284.6 eV corresponds to the C–C bonds in the carbon network, while the weaker ones at 285.9, 287.4, and 289.2 eV indicate the existence of some residual oxygen-containing functional groups from the insufficient reduction/carbonization of organic substances at a relatively low temperature (500 °C).[33] The typical Raman shifts of MnO (~362 and 645 cm^{-1}) and C (~1340 and 1585 cm^{-1}) can also been probed in the Raman spectrum (Figure 1d),[26] which is quite consistent with the XPS results. The presence of a D-band with high intensity suggests the existence of nongraphitic carbon, which possesses significantly more Li storage sites than graphitic carbon.[46,47] The carbon content in the MnO-MICN product evaluated by TGA is ~12.7 wt % (see Figure S1 in the Supporting Information).

The morphology and structure of the 3D MnO-MICN product were further studied by FESEM and TEM. Figure 2a displays the FESEM image of the 3D MnO-MICN product. It is observed that a large number of particles with sizes of ~200 nm exist in the product. They are connected to each other to form an interconnected network. The FESEM image at a higher magnification (Figure 2b) clearly reveals that these particles are composed of ultrafine nanocrystals ~16 nm in size. The TEM images (Figure 2c and 2d) further verify that the 3D MnO-

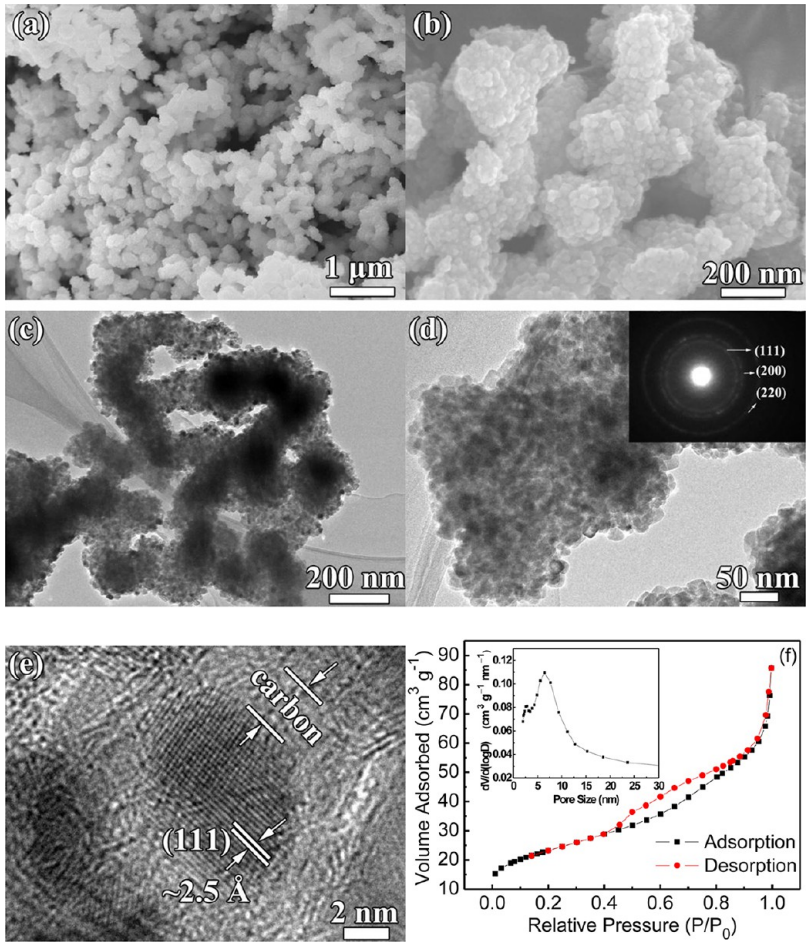

Figure 2. (a, b) Field-emission scanning electron microscopy (FESEM) and (c, d) transmission electron microscopy (TEM) images of MnO-MICN; inset of panel (d) shows the related SAED pattern. (e) Typical high-resolution transmission electron microscopy (HRTEM) image of MnO-MICN. (f) Nitrogen adsorption and desorption isotherm of MnO-MICN (inset shows the pore size distribution).

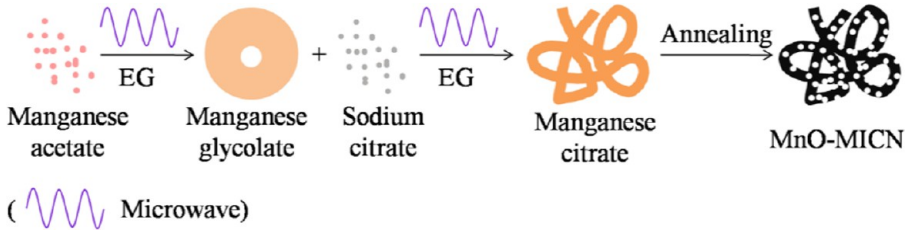

Figure 3. Schematic illustration of the formation process of MnO-MICN.

Table 1. Detailed Experimental Conditions and Morphologies of the Mn-Based Precursors Synthesized Using Different Contents of Sodium Citrate

sample	sodium citrate content (mmol)	morphology
a	0	micrometer-sized rings
b	0.05	submicrometer spheres assembled by nanodisks
c	0.1	submicrometer spheres + chainlike products
d	0.3	chainlike products assembled by nanoparticles
e	0.6	interconnected network assembled by nanoparticles
f	1	interconnected network assembled by nanoparticles

MICN comprises considerable MnO nanoparticles homogeneously encapsulated in a mesoporous carbon matrix with pore sizes in the range of 3−10 nm. Meanwhile, the mesoporous carbon matrix forms an interconnected network, which is beneficial to facilitate the contact of electrolyte with active material and the transport of electrons and Li^+ ions.[36,48] In addition, Figure 2d exhibits obvious diffraction rings, indicating the polycrystalline nature of the 3D MnO-MICN nanoarchitecture. The diffraction rings are assigned to the (111), (200), and (220) planes of MnO, which is consistent with the XRD result (Figure 1a). Figure 2e shows the HRTEM image for an individual MnO particle encapsulated within an amorphous carbon layer with a thickness of 2−3 nm. The *d*-spacing of the planes in the lattice is ~2.5 Å and corresponds to the (111) plane of MnO. The successful synthesis of MnO-MICN was further confirmed by the elemental signatures of

dx.doi.org/10.1021/am302813d | ACS Appl. Mater. Interfaces 2013, 5, 1997−2003

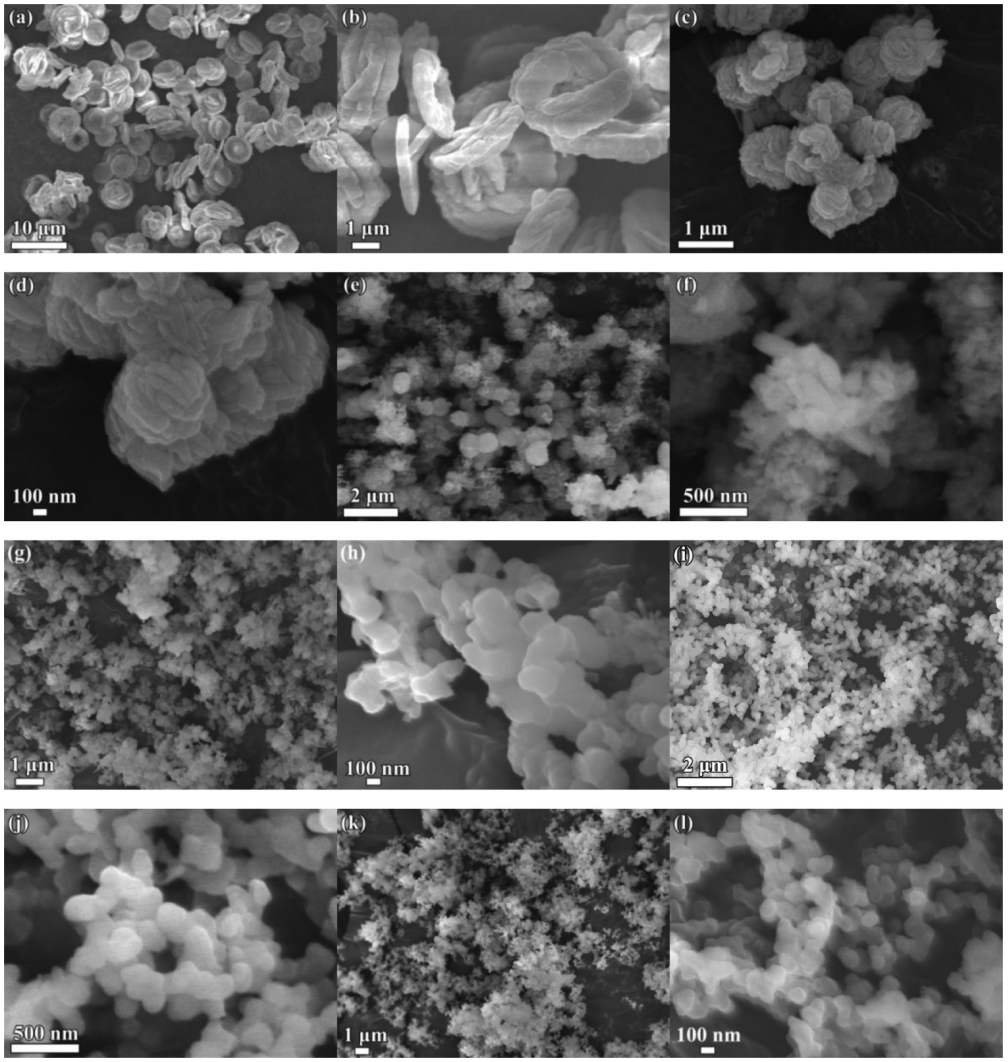

Figure 4. FESEM images of the Mn-based precursors synthesized under conditions listed in Table 1: (a, b) sample a, (c, d) sample b, (e, f) sample c, (g, h) sample d, (i, j) sample e, and (k, l) sample f.

Mn, O, and C in the energy-dispersive X-ray (EDX) spectrum (see Figure S2 in the Supporting Information). Also, the EDX elemental mapping (see Figure S3 in the Supporting Information) suggests that the MnO nanoparticles are encapsulated well within the mesoporous interconnected carbon network.

The mesoporous nature of the 3D MnO-MICN product is further confirmed by nitrogen adsorption−desorption measurements. Figure 2f displays the isothermal plot of the MnO-MICN product, which is a typical type IV isotherm representing a mesoporous structure with a Brunauer−Emmett−Teller (BET) specific surface area as high as 82.7 $m^2 g^{-1}$. The pore size distribution shown in the inset of Figure 2f suggests that the 3D MnO-MICN product has numerous mesopores ~2.8 and 7.6 nm in diameter, in agreement with the TEM observations. Such a high specific surface area and quite numerous mesopores are able to promote efficient and equal access of the electrolyte to the internal active materials.[46] Meanwhile, the mesoporous carbon network with mutual interconnection in all the directions can not only buffer the volume change, but also ensure a continuous conductive network for the fast electron and Li-ion transportation, thus resulting in high rate capability and excellent cycle performance when they are applied to lithium storage.[33]

Figure 3 outlines a plausible reaction process for the formation of 3D MnO-MICN, where the ligand exchange between glycolate and citrate should be the key step. In order to clearly understand the ligand exchange, experiments using different contents of SC were carried out (Table 1). First, the acetate functional groups of MA were replaced by EG groups in the absence of SC, resulting in the formation of manganese glycolate. The reaction process of manganese glycolate has been clearly demonstrated in the previous reports on the similar metal glycolates.[49−55] Upon the introduction of SC, the citrate functional groups gradually replace the glycolate in the manganese glycolate, because the coordination ability of citrate to metal ions through the carboxyl groups is stronger than that of glycolate.[56,57] This proposed process was well confirmed by the gradual enhance of citrate signals and the fading of glycolate peaks in the Fourier transform infrared (FTIR) spectra and XRD patterns with increasing SC (see Figures S4 and S5 in the Supporting Information).

FESEM images of the Mn-based precursors synthesized using different contents of SC (Figure 4) also indicate the morphology evolution. As shown in Figures 4a and 4b, the

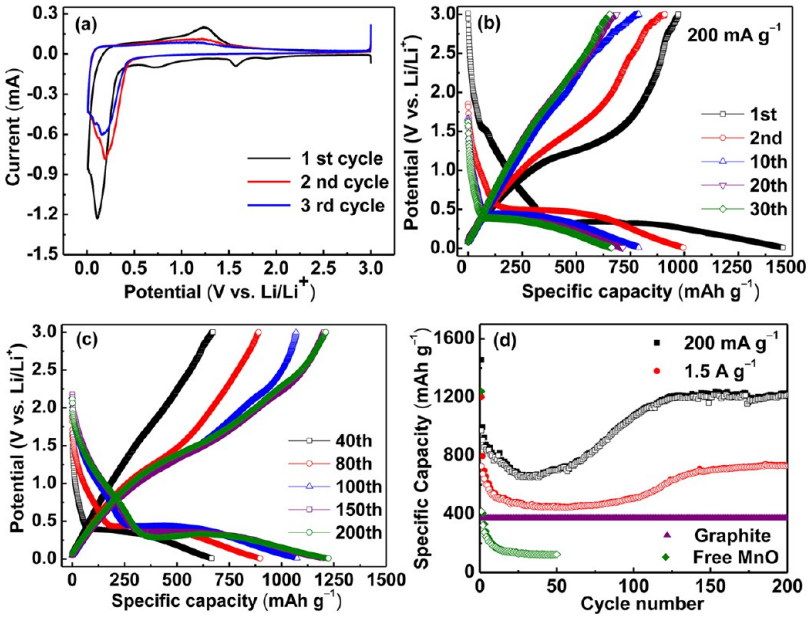

Figure 5. (a) Typical first three cyclic voltammograms of the MnO-MICN electrode at a scanning rate of 0.1 mV s^{-1} in the range of 0.01−3 V. Galvanostatic discharge/charge curves of the MnO-MICN electrode at a current density of 200 mA g^{-1} in the range of 0.01−3 V ((b) 1st, 2nd, 10th, 20th, and 30th cycles; and (c) the 40th, 80th, 100th, 150th, and 200th cycles). (d) Capacity−cycle number curves and rate performances of MnO-MICN and free MnO nanoparticles.

product of manganese glycolate consists of micrometer-sized rings ∼3 μm in diameter and ∼200 nm thick, which is a common morphology for the metal glycolates.[52] With the introduction of a small amount of SC (0.05 mmol), however, spherical particles 0.6−1 μm in size are formed (see Figures 4c and 4d). These spherical particles were composed of 100-nm-thick nanodisks, partially inheriting the morphology of the manganese glycolate intermediate. When the content of SC is increased to 0.1 mmol, some chainlike structures that are made from nanorods ∼100 nm in width and ∼300 nm in length are generated, although the spherical particles still exist (see Figures 4e and 4f). As the content of SC further increases, the chainlike structures in the products become the majority, and the nanorods transform to interconnected nanoparticles with a diameter of ∼200 nm (see Figures 4g−4l). Under a controlled calcination treatment, the organic species in the precursors can be easily transformed to interconnected carbon network with considerable mesopores. Also, they may prevent effectively from the overgrowth and overagglomeration of MnO, leading to nanosized MnO uniformly encapsulated in the mesoporous interconnected carbon network (Figure 2). Compared with the previous methods for building hierarchical mixed-conducting networks, the present work may provide a more economical route for large-scale production of metal oxides embedded in the interconnected carbon matrix.

The electrochemical lithium-storage properties of the as-prepared 3D MnO-MICN have been further explored. Figure 5a displays representative CV curves of the electrode made of the 3D MnO-MICN. In the first cycle, a reduction peak at ∼1.5 V can be assigned to the reduction of Mn^{3+} or Mn^{4+} to Mn^{2+}, which could have originated from a trace Mn_xO_y impurity from the partial oxidation of the Mn^{2+} in the product.[15] In addition, a reduction peak near 0.71 V corresponds to the irreversible reduction of electrolyte and the formation of a solid electrolyte interphase (SEI) layer. Furthermore, the sharp cathodic peak close to 0.11 V corresponds to the complete reduction of Mn^{2+} to Mn^0, which shifts to 0.2 V in the subsequent cycles. In the anodic process, a broad oxidation peak observed at 1.23 V could be ascribed to the Mn^0 to Mn^{2+}. Figure 5b shows the typical discharge and charge curves of the MnO-MICN electrode at a current density of 200 mA g^{-1} over a potential range between 0.01 and 3 V. The overall discharge capacity in the first discharge process is as high as 1456 mA h g^{-1}, which is much higher than the theoretical value (755 mA h g^{-1}) of MnO based on the conversion reaction. From the second cycle on, both of the discharge and charge curves gradually become shorter, presenting a common capacity fading. Interestingly, the curves start to recover after 40 cycles. In particular, it is worth noting that a slope of 1.5−2.3 V in the charge process gradually appears after ∼100 cycles, which may originate from the new electrochemical reaction. For instance, Mn^{2+} may be oxidized to a higher oxidation state. More importantly, the new slope in the charge process and the corresponding drop in potential from 2 V to the potential of plateau could significantly enhance the specific capacity (∼30% of the overall capacity). After 200 cycles at 200 mA g^{-1}, the discharge capacity reaches 1224 mA h g^{-1} with a Coulombic efficiency of ∼99% (see Figure S6 in the Supporting Information), indicating an excellent cyclic performance. Combining with the phenomenon of capacity fading and recovering, the cycling behavior of the 3D MnO-MICN electrode exhibits a "U" shape (Figure 5d), which has also been observed in other nanostructured Mn-based oxides.[58−61] Also, the MnO-MICN electrode cycled at a high current density of 1500 mA g^{-1} exhibits similar behavior (see Figure S7 in the Supporting Information). A high specific discharge capacity of 731 mA h g^{-1} is retained after 200 cycles at the current density of 1500 mA g^{-1} (Figure 5d), exhibiting a superior rate capability. As suggested by previous reports,[59,62−64] the conversion−reaction kinetics can be improved by the formation of defects in the electrodes during cycling, leading to the oxidation of Mn^{2+} to a higher oxidation state and the appearance of a unique "U" shape. Of course, this issue

must be further explored, although the phenomenon of a gradual increase in capacity is also common in other TMO anodes. In a control experiment, we synthesized free MnO nanoparticles by subjecting MA to direct thermal treatment, based on the same heating conditions for the MnO-MICN. The pure MnO phase was confirmed by XRD and Raman analyses (see Figure S8 in the Supporting Information). The FESEM images depicted in Figure S9 in the Supporting Information show that the particle size of the free MnO nanoparticles ranges from 20 nm to 30 nm. However, the electrochemical performance of the electrode made of these free MnO nanoparticles is much worse than that of the MnO-MICN product. Although the electrode made of the free MnO nanoparticles displays a high initial discharge capacity of 1239 mA h g^{-1} at a low current density of 100 mA g^{-1}, it decays rapidly to 178 mA h g^{-1} after only 10 cycles (see Figure 5d). Furthermore, the EIS spectra of the electrodes were investigated (see Figure S10 in the Supporting Information). The MnO-MICN exhibits a much lower resistance than the MnO nanoparticles, which could be attributed to the unique mesoporous interconnected carbon network. Also, the morphology of the active materials in the electrode upon cycling was investigated by TEM. Interestingly, the initial structure was basically maintained after 100 cycles at a current density of 1500 mA g^{-1} (see Figure S11 in the Supporting Information).

CONCLUSIONS

In summary, we have successfully developed a facile method based on a rapid microwave-polyol process to synthesize ultrafine MnO nanoparticles encapsulated in a three-dimensional (3D) mesoporous interconnected carbon network in large quantities for the first time. The effects of sodium citrate on the morphology of the Mn-based precursors were investigated systematically. The as-prepared 3D MnO-MICN exhibits high reversible capacity, excellent cyclability, and superior rate capability, because of its unique structure. Besides, the strategy based on the use of MICN as a structure support and a conductive medium for transition-metal oxide (TMO) nanoparticles can be potentially generalized for improving the performance of other electrode materials in lithium-ion batteries.

ASSOCIATED CONTENT

Supporting Information

TGA curve, FESEM and TEM images, EDX, elemental mapping analyses, XRD patterns, Raman spectrum, Columbic efficiency, discharge/charge curves, and EIS spectra. This material is available free of charge via the Internet at http://pubs.acs.org.

AUTHOR INFORMATION

Corresponding Author

*Fax: +86-27-87558241. E-mail addresses: huxl@mail.hust.edu.cn (X.L.H.), huangyh@mail.hust.edu.cn (Y.H.).

Notes

The authors declare no competing financial interest.

ACKNOWLEDGMENTS

This work was supported by the Natural Science Foundation of China (Grant Nos. 21271078, 51002057, and 50825203) and the PCSIRT (Program for Changjiang Scholars and Innovative Research Team in University). The authors thank Analytical and Testing Center of HUST for the XRD and TGA measurements.

REFERENCES

(1) Tarascon, J. M.; Armand, M. *Nature* **2001**, *414*, 359−367.
(2) Whittingham, M. S. *Chem. Rev.* **2004**, *104*, 4271−4301.
(3) Yuan, L. X.; Wang, Z. H.; Zhang, W. X.; Hu, X. L.; Chen, J. T.; Huang, Y. H.; Goodenough, J. B. *Energy Environ. Sci.* **2011**, *4*, 269−284.
(4) Chan, C. K.; Peng, H. L.; Liu, G.; McIlwrath, K.; Zhang, X. F.; Huggins, R. A.; Cui, Y. *Nat. Nanotechnol.* **2008**, *3*, 31−35.
(5) Besenhard, J. O.; Yang, J.; Winter, M. *J. Power Sources* **1997**, *68*, 87−90.
(6) Winter, M.; Besenhard, J. O. *Electrochim. Acta* **1999**, *45*, 31−50.
(7) Poizot, P.; Laruelle, S.; Grugeon, S.; Tarascon, J. M. *J. Electrochem. Soc.* **2002**, *149*, A1212−A1217.
(8) Poizot, P.; Laruelle, S.; Grugeon, S.; Dupont, L.; Tarascon, J. M. *Nature* **2000**, *407*, 496−499.
(9) Lou, X. W.; Deng, D.; Lee, J. Y.; Feng, J.; Archer, L. A. *Adv. Mater.* **2008**, *20*, 258−262.
(10) Hu, H. B.; Chen, J. S.; Hng, H. H.; Lou, X. W. *Nanoscale* **2012**, *4*, 2526−2542.
(11) Guo, B. K.; Fang, X. P.; Li, B.; Shi, Y. F.; Ouyang, C. Y.; Hu, Y. S.; Wang, Z. X.; Stucky, G. D.; Chen, L. Q. *Chem. Mater.* **2011**, *24* (3), 457−463.
(12) Fang, X. P.; Guo, B. K.; Shi, Y. F.; Li, B.; Hua, C. X.; Yao, C. H.; Zhang, Y. C.; Hu, Y. S.; Wang, Z. X.; Stucky, G. D.; Chen, L. Q. *Nanoscale* **2012**, *4* (5), 1541−1544.
(13) Fang, X. P.; Lu, X.; Guo, X. W.; Mao, Y.; Hu, Y. S.; Wang, J. Z.; Wang, Z. X.; Wu, F.; Liu, H. K.; Chen, L. Q. *Electrochem. Commun.* **2010**, *12*, 1520−1523.
(14) Zhong, K. F.; Xia, X.; Zhang, B.; Li, H.; Wang, Z. X.; Chen, L. Q. *J. Power Sources* **2010**, *195*, 3300−3308.
(15) Sun, B.; Chen, Z. X.; Kim, H. S.; Ahn, H.; Wang, G. X. *J. Power Sources* **2011**, *196*, 3346−3349.
(16) Yu, X. Q.; He, Y.; Sun, J. P.; Tang, K.; Li, H.; Chen, L. Q.; Huang, X. J. *Electrochem. Commun.* **2009**, *11*, 791−794.
(17) Li, X. W.; Li, D.; Qiao, L.; Wang, X. H.; Sun, X. L.; Wang, P.; He, D. Y. *J. Mater. Chem.* **2012**, *22*, 9189−9194.
(18) Zhong, K. F.; Zhang, B.; Luo, S. H.; Wen, W.; Li, H.; Huang, X. J.; Chen, L. Q. *J. Power Sources* **2011**, *196*, 6802−6808.
(19) Xu, G. L.; Xu, Y. F.; Sun, H.; Fu, F.; Zheng, X. M.; Huang, L.; Li, J. T.; Yang, S. H.; Sun, S. G. *Chem. Commun.* **2012**, *48*, 8502−8504.
(20) Kokubu, T.; Oaki, Y.; Hosono, E.; Zhou, H. S.; Imai, H. *Adv. Funct. Mater.* **2011**, *21*, 3673−3680.
(21) Liu, J.; Pan, Q. M. *Electrochem. Solid State Lett.* **2010**, *13*, A139−A142.
(22) Ding, Y. L.; Wu, C. Y.; Yu, H. M.; Xie, J.; Cao, G. S.; Zhu, T. J.; Zhao, X. B.; Zeng, Y. W. *Electrochim. Acta* **2011**, *56*, 5844−5848.
(23) Liu, Y. M.; Zhao, X. Y.; Li, F.; Xia, D. G. *Electrochim. Acta* **2011**, *56*, 6448−6452.
(24) Hsieh, C. T.; Lin, C. Y.; Lin, J. Y. *Electrochim. Acta* **2011**, *56*, 8861−8867.
(25) Liu, S. Y.; Xie, J.; Zheng, Y. X.; Cao, G. S.; Zhu, T. J.; Zhao, X. B. *Electrochim. Acta* **2012**, *66*, 271−278.
(26) Zhang, K.; Han, P.; Gu, L.; Zhang, L.; Liu, Z.; Kong, Q.; Zhang, C.; Dong, S.; Zhang, Z.; Yao, J.; Xu, H.; Cui, G.; Chen, L. Q. *ACS Appl. Mater. Interfaces* **2012**, *4*, 658−664.
(27) Herle, P. S.; Ellis, B.; Coombs, N.; Nazar, L. F. *Nat. Mater.* **2004**, *3*, 147−152.
(28) Li, X. L.; Kang, F. Y.; Bai, X. D.; Shen, W. C. *Electrochem. Commun.* **2007**, *9*, 663−666.
(29) Zheng, S. F.; Hu, J. S.; Zhong, L. S.; Song, W. G.; Wan, L. J.; Guo, Y. G. *Chem. Mater.* **2008**, *20*, 3617−3622.
(30) Ban, C. M.; Wu, Z. C.; Gillaspie, D. T.; Chen, L.; Yan, Y. F.; Blackburn, J. L.; Dillon, A. C. *Adv. Mater.* **2010**, *22*, 145−149.

(31) Wang, H.; Cui, L. F.; Yang, Y.; Sanchez Casalongue, H.; Robinson, J. T.; Liang, Y.; Cui, Y.; Dai, H. J. *J. Am. Chem. Soc.* **2010**, *132*, 13978−13980.
(32) Ding, S. J.; Luan, D. Y.; Boey, F. Y. C.; Chen, J. S.; Lou, X. W. *Chem. Commun.* **2011**, *47*, 7155−7157.
(33) Sun, Y. M.; Hu, X. L.; Luo, W.; Huang, Y. H. *ACS Nano* **2011**, *5*, 7100−7106.
(34) Guo, Y. G.; Hu, Y. S.; Sigle, W.; Maier, J. *Adv. Mater.* **2007**, *19*, 2087−2091.
(35) Hu, Y. S.; Guo, Y. G.; Dominko, R.; Gaberscek, M.; Jamnik, J.; Maier, J. *Adv. Mater.* **2007**, *19*, 1963−1966.
(36) Hu, Y. S.; Liu, X.; Müller, J. O.; Schlögl, R.; Maier, J.; Su, D. S. *Angew. Chem., Int. Ed.* **2009**, *48*, 210−214.
(37) Komarneni, S. *Curr. Sci.* **2003**, *85*, 1730−1734.
(38) Galema, S. A. *Chem. Soc. Rev.* **1997**, *26*, 233−238.
(39) Tsuji, M.; Hashimoto, M.; Nishizawa, Y.; Kubokawa, M.; Tsuji, T. *Chem.—Eur. J.* **2005**, *11*, 440−452.
(40) Zhu, Y. J.; Wang, W. W.; Qi, R. J.; Hu, X. L. *Angew. Chem., Int. Ed.* **2004**, *116*, 1434−1438.
(41) Panda, A. B.; Glaspell, G.; El-Shall, M. S. *J. Am. Chem. Soc.* **2006**, *128*, 2790−2791.
(42) Hu, X. L.; Yu, J. C. *Chem. Mater.* **2008**, *20* (21), 6743−6749.
(43) Hu, X. L.; Yu, J. C.; Gong, J. M.; Li, Q.; Li, G. S. *Adv. Mater.* **2007**, *19*, 2324−2329.
(44) Hu, X. L.; Gong, J. M.; Zhang, L. Z.; Yu, J. C. *Adv. Mater.* **2008**, *20*, 4845−4850.
(45) Hu, X. L.; Yu, J. C. *Adv. Funct. Mater.* **2008**, *18*, 880−887.
(46) Ji, X. L.; Herle, P. S.; Rho, Y.; Nazar, L. F. *Chem. Mater.* **2007**, *19*, 374−383.
(47) Luo, W.; Hu, X. L.; Sun, Y. M.; Huang, Y. H. *Phys. Chem. Chem. Phys.* **2011**, *13*, 16735−16740.
(48) Luo, W.; Hu, X. L.; Sun, Y. M.; Huang, Y. H. *J. Mater. Chem.* **2012**, *22*, 8916−8921.
(49) Scott, R. W. J.; Coombs, N.; Ozin, G. A. *J. Mater. Chem.* **2003**, *13*, 969−974.
(50) Wang, Y.; Jiang, X.; Xia, Y. N. *J. Am. Chem. Soc.* **2003**, *125*, 16176−16177.
(51) Jiang, X.; Wang, Y.; Herricks, T.; Xia, Y. N. *J. Mater. Chem.* **2004**, *14*, 695−703.
(52) Chakroune, N.; Viau, G.; Ammar, S.; Jouini, N.; Gredin, P.; Vaulay, M. J.; Fievet, F. *New J. Chem.* **2005**, *29*, 355−361.
(53) Cao, A. M.; Hu, J. S.; Liang, H. P.; Wan, L. J. *Angew. Chem., Int. Ed.* **2005**, *44*, 4391−4395.
(54) Zhong, L. S.; Hu, J. S.; Liang, H. P.; Cao, A. M.; Song, W. G.; Wan, L. J. *Adv. Mater.* **2006**, *18*, 2426−2429.
(55) Wang, X.; Wu, X. L.; Guo, Y. G.; Zhong, Y.; Cao, X.; Ma, Y.; Yao, J. N. *Adv. Funct. Mater.* **2010**, *20* (10), 1680−1686.
(56) Zhang, G.; Yu, L.; Wu, H. B.; Hoster, H. E.; Lou, X. W. *Adv. Mater.* **2012**, *24*, 4609−4613.
(57) Zhong, Y.; Wang, X.; Jiang, K.; Zheng, J. Y.; Guo, Y.; Ma, Y.; Yao, J. N. *J. Mater. Chem.* **2011**, *21*, 17998−18002.
(58) Sun, Y. M.; Hu, X. L.; Luo, W.; Huang, Y. H. *J. Mater. Chem.* **2012**, *22*, 19190−19195.
(59) Guo, J. C.; Liu, Q.; Wang, C. S.; Zachariah, M. R. *Adv. Funct. Mater.* **2012**, *22*, 803−808.
(60) Courtel, F. M.; Duncan, H.; Abu-Lebdeh, Y.; Davidson, I. J. *J. Mater. Chem.* **2011**, *21*, 10206−10218.
(61) Zhou, L.; Wu, H. B.; Zhu, T.; Lou, X. W. *J. Mater. Chem.* **2012**, *22*, 827−829.
(62) Feng, J. K.; Song, B. H.; Lai, M. O.; Lu, L. *Funct. Mater. Lett.* **2012**, *05*, 1250028.
(63) Lu, Q.; Zhou, Y. K. *Funct. Mater. Lett.* **2011**, *4*, 31−36.
(64) Sun, Y. M.; Hu, X. L.; Luo, W.; Huang, Y. H. *Adv. Funct. Mater.* **2012**, DOI: 10.1002/adfm.201202623.